In situ Raman and Time-Resolved Luminescence Investigation of Local Structure of ZrO2 in the Amorphous to Crystalline Phase Transition

6 AUTHORS, INCLUDING:

Carmen Tiseanu

National Institute for Laser, Plasma and Radia…

66 PUBLICATIONS **613** CITATIONS

SEE PROFILE

Bogdan Cojocaru

University of Bucharest

37 PUBLICATIONS **484** CITATIONS

SEE PROFILE

Kelly Pemartin

7 PUBLICATIONS **40** CITATIONS

SEE PROFILE

Margarita Sanchez-Dominguez

Centro de Investigación en Materiales Avanza…

52 PUBLICATIONS **582** CITATIONS

SEE PROFILE

In situ Raman and Time-Resolved Luminescence Investigation of the Local Structure of ZrO$_2$ in the Amorphous to Crystalline Phase Transition

Carmen Tiseanu,*,[†] Vasile I. Parvulescu,[‡] Bogdan Cojocaru,[‡] Kelly Pemartin,[§]
Margarita Sanchez-Dominguez,[§,‖] and Magali Boutonnet[⊥]

[†]National Institute for Laser, Plasma and Radiation Physics, P.O. Box MG-36, RO 76900, Bucharest-Magurele, Romania

[‡]University of Bucharest, Department of Chemical Technology and Catalysis 4 − 12 Regina Elisabeta Bvd., Bucharest 030016, Romania

[§]National Institute for Laser, Plasma and Radiation Physics, Instituto de Química Avanzada de Cataluña, Consejo Superior de Investigaciones Científicas (IQAC-CSIC), CIBER en Biotecnología, Biomateriales y Nanomedicina (CIBER BBN), Jordi Girona 18-26, 08034 Barcelona, Spain

[‖]Centro de Investigación en Materiales Avanzados, S. C. (CIMAV), Unidad Monterrey, GENES-Group of Embedded Nanomaterials for Energy Scavenging, Alianza Norte 202, Parque de Investigación e Innovación Tecnológica, 66600 Apodaca, Nuevo León, Mexico

[⊥]Kungliga Tekniska Högskolan (KTH), School of Chemistry, Div. of Chemical Technology, Teknikringen 42, SE-10044, Stockholm, Sweden

S *Supporting Information*

ABSTRACT: The local structure of europium doped and impregnated ZrO$_2$ in the amorphous state and during crystallization is investigated by *in situ* X-ray diffraction and *in situ* Raman, high-resolution transmission electron microscopy (HRTEM) and time-resolved photoluminescence spectroscopy. From Raman spectra excited at three different wavelengths (λ_{ex}= 488, 514, and 633 nm), both phonon modes of ZrO$_2$ and photoluminescence (PL) corresponding to europium electronic transitions were investigated. In the as-synthetized state, samples were X-ray and Raman amorphous with few tetragonal (also monoclinic) crystallites being observed under HRTEM microscopy. *In situ* XRD patterns

show that all samples crystallize in the tetragonal phase around 450 °C. The time-resolved PL spectra of europium doped and impregnated ZrO$_2$ show spectral dynamics with time delay after lamp/laser pulse which is assigned to the coexistence of the different amorphous and crystalline components or unreacted europium precursor. From *in situ* Raman spectra, crystallization was detected at 300−350 °C, monitoring for the characteristic tetragonal-like $^5D_0-^7F_2$ emission of europium at 606 nm. The ratio of tetragonal to amorphous emission increased abruptly from ca. 2−4% at 300−400 °C to almost 25% at 400−450 °C, whereas at 500 °C the emission is mostly tetragonal. A similar trend was found with the *ex situ* calcined samples, but relative strong tetragonal emission was observed at lower temperature in the range of 350 to 400 °C.
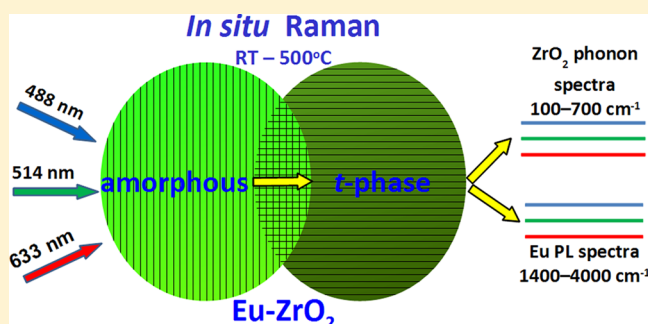
1. INTRODUCTION

Pure zirconia (ZrO$_2$) exists in three distinct polymorphic phases (monoclinic, tetragonal, and cubic), which are closely related to the cubic fluorite structure.[1−10] In general, the monoclinic form is the stable phase at room temperature, whereas, at elevated temperatures (>1170 °C), the tetragonal phase becomes stable, followed by the cubic phase at even higher temperatures (>2370 °C). Upon doping with different trivalent cations such as Y^{3+} or lanthanides (Ln^{3+}), the cubic and tetragonal phases can be stabilized at lower or even ambient temperatures.[2,4−6] The evolution of structural and electronic properties of Y^{3+}/Ln^{3+} doped zirconia as a function of factors such as ion type and concentration, synthesis method,

and temperature of treatment has been intensively studied in recent years, since these can be very relevant for their potential applications as solid oxide fuel cells, oxygen sensors, electrolytes, and composite electrodes.[11−13] Furthermore, many lanthanide-doped zirconia-based materials have the potential to be used for Vis to NIR/white photoluminescence (PL)-based applications.[14−20]

Because the main structural difference between zirconia phases is given by the displacements of the oxygen atoms in the

lattices, consideration of the local atomic structure is essential to fully understand the effect of doping on ZrO_2.[10] Laser-excited Raman spectra are locally sensitive to Zr−O bonds in the first (0.1−0.5 nm) and second (0.5−5 nm) atomic shells and also to the lattice defects. Photoluminescence in combination with europium (Eu^{3+}) as a structural probe represents also a powerful short-range sensitive technique. The luminescence properties of europium are very sensitive to changes of the first coordination sphere; i.e., it shows strongly different emission spectra and excited state dynamics depending on its local symmetry, i.e., cubic, tetragonal, or monoclinic structure.[21−30] Also, in comparison with Raman spectroscopy, surface and/or disordered type environments can be easily discriminated with luminescence.

Although ZrO_2 have been extensively investigated both experimentally and theoretically in the crystalline phases, there is little work reported on the amorphous phase.[8] With very few exceptions, luminescence studies regarding lanthanide doped ZrO_2 regard crystalline states obtained upon calcination at high temperatures.[21,30] The present work proposes *in situ* XRD and *in situ* Raman, HRTEM, and time-resolved PL investigation to describe and understand the local structure at europium sites in nanostructured ZrO_2 in the amorphous state and its evolution during crystallization. Luminescence was either measured via pulsed lamp/laser excitation (*ex situ* luminescence) or extracted from *in situ* Raman spectra (*in situ* luminescence). For this, Raman spectra were measured within the extended spectral region from 150 to 800 cm^{-1} (where the typical phonon modes of ZrO_2 polymorphs lie) up to 4000 cm^{-1}. To our knowledge, there are no studies concerning *in situ* combined Raman and luminescence of europium, though properties of zirconia measured beyond the phonon spectral region were reported in the literature.[31−33] Bettinelli et al. performed extensive laser-excited Raman and luminescence spectroscopy of a series of ceria−zirconia mixed oxides, containing trivalent lanthanide ions as *unintentional impurities*, using 488, 514.5, and 1064 nm excitation wavelengths.[31] It was found that the bands located at Stokes shifts higher than 800 cm^{-1} from the laser lines relate to f−f emission transitions of Pr^{3+}, Nd^{3+}, Ho^{3+}, and Er^{3+} ions. A relative intense electronic Raman peak at 2086 cm^{-1} was observed in the resonant Raman spectra of cerium-doped yttria-stabilized ZrO_2 single crystals. This line was assigned to the $^2F_{7/2} \rightarrow {}^2F_{5/2}$ electronic transition within the $4f^1$ configuration of Ce^{3+}.[32] According to spectroscopic investigation of Meijerink et al. on dynamically compacted monoclinic ZrO_2 with various dopants including Sm^{3+}, the extra Raman lines observed at 488 nm excitation in the spectral range 1850−3000 cm^{-1} were related to the f−f electronic transitions of Sm^{3+} ions.

To overcome the limitation of single laser excitation in discriminating the emission of intentionally doped europium from the unintentionally present impurities,[31] three different excitation wavelengths (λ_{ex} = 488, 514, and 633 nm) were used. Europium doped and impregnated ZrO_2 were synthetized by a novel oil-in-water microemulsion reaction method.[34−36] We show that, by use of combined *in situ* Raman and luminescence with temperature and *ex situ* time-resolved luminescence, the knowledge on the local structure of lanthanide doped host in the amorphous state and during crystallization is improved.

2. EXPERIMENTAL METHODS

2.1. Materials and Preparation. Synperonic 10/6 was a gift from Croda. Zirconium(IV) 2-ethylhexanoate was from Alfa Aesar; europium(III) 2-ethylhexanoate was purchased from Strem Chemicals. Hexane (Suprasolv, for gas chromatography) and ammonia 30% were purchased from Merck. Isopropanol was purchased from Carlo Erba. The employed microemulsion system was water/Synperonic10/6/hexane. The zirconium(IV) 2-ethylhexanoate and europium(III) 2-ethylhexanoate represent the organometallic sources of Zr and Eu, respectively. Because the microemulsion used is oil-in-water, the precursor should be soluble in the oil phase (hexane) in order to be confined in the interior of the nanoscale droplets.

The composition of the microemulsion was 64.5 wt % water, 21.5 wt % surfactant, and 14 wt % oil phase, which was a hexane solution of zirconium(IV) 2-ethylhexanoate for the synthesis of undoped zirconia (ZE), while for Eu bulk-doped zirconia (ZEB) the oil phase was a hexane solution of zirconium(IV) 2-ethylhexanoate and europium(III) 2-ethylhexanoate (0.99:0.01 Zr/Eu atomic ratio). The preparation of the nanoparticles by the o/w microemulsion reaction approach was carried out as follows. All the components were mixed to obtain an isotropic solution (microemulsion) at a temperature of 35 °C. The pH of the solution was then increased to 11 by addition of concentrated ammonia under vigorous stirring and left for 48 h. The obtained zirconia precipitate was washed by a mixture of ethanol and chloroform (1:1), dried overnight at 70 °C, and grinded using an agate pestle and mortar. For the impregnated samples (obtained via wetness impregnation), 1 g of ZrO_2 was impregnated with 16.4 mL of a 0.004 M europium(III) 2-ethylhexanoate solution. Drying of the samples was carried out using the same protocol as for the doped material. All samples were calcined under air *in situ* (during the XRD and Raman experiments up to 1000 and 500 °C, respectively) and *ex situ* at 500 °C at a heating rate of 1−2 °C/min. The dried pure, europium-doped, and impregnated ZrO_2 were denoted as ZE, ZEB, and ZEI, respectively. The thermally treated samples are denoted as ZE-T/ZEB-T/ZEI-T, where T holds for the value of temperature (°C).

2.2. Characterization. Particle size and morphology were investigated by high resolution transmission electron microscopy (HRTEM). The sample was prepared as follows: 0.5 mg of zirconia powder was suspended in isopropanol (2 mL) and sonicated. For analysis, a drop of this dispersion was deposited onto a holey Formvar/carbon copper grid. Observation was carried out using a field emission transmission electron microscope, JEM-2200FS, 200 kV, with 0.19 nm resolution in TEM mode and 0.1 nm resolution in STEM mode and spherical aberration correction in STEM mode.

Powder X-ray diffraction (XRD) patterns were recorded on a Schimadzu XRD-7000 diffractometer using Cu Kα radiation (λ = 1.5418 Å, 40 kV, 40 mA) at a scanning speed of 0.10 deg min^{-1} in the 6−60° 2Θ range inside an *in situ* cell accessory. *In situ* calcination of the samples was carried out using the same apparatus in the 50−500 °C temperature range. Raman analysis was carried out with a Horiba Jobin Yvon - Labram HR UV−visible-NIR Raman microscope spectrometer, at 633, 514, and 488 nm and a catalytic cell for sample heating. The analysis was carried out under the following conditions: beam diameter of 1.0 + 5% mm, spot diameter of 0.5 μm for *ex situ* measurements and 1.5 μm for *in situ* measurements, and spatial resolution of 0.35 μm for *ex situ* measurements and 0.6 μm for *in situ* measurements. *In situ* measurements were carried out in the range 50−550 °C by heating the samples with a rate of 10 °C/min and keeping a plateau of 10 min for collecting the spectra. Fourier transform infrared (FTIR) spectra were measured with a Thermo Electron Nicolet 4700 FTIR spectrometer with a
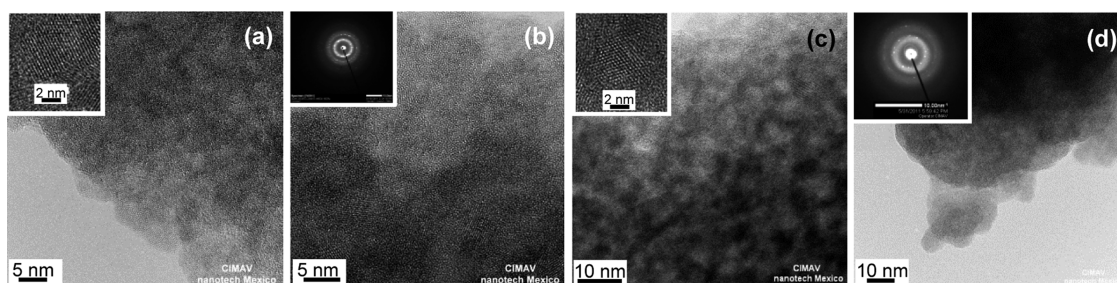
Figure 1. TEM images of ZE (a, b) and ZEB (c, d). The insets to parts a and c are HRTEM images, and the insets to parts b and d are corresponding SAED patterns.

Smart Accessory for diffuse reflectance measurements. The IR spectra were scanned in the region 4000−400 cm^{-1} at a resolution of 4 cm^{-1}. The final spectra are an accumulation of 200 scans.

2.3. Photoluminescence Measurements. The photoluminescence (PL) measurements were carried out using a Fluoromax 4 spectrofluorometer (Horiba) operated in both the fluorescence and phosphorescence modes. The repetition rate of the xenon flash lamp was 25 Hz, the integration window varied between 300 ms and 3 s, the delay after flash varied between 0.03 and 10 ms, and up to 100 flashes were accumulated per data point. Time resolved emission spectra (TRES) were recorded at room temperature using a wavelength tunable Nd:YAG-laser/OPO system (Spectra Physics/GWU) operated at 20 Hz as the excitation light source and an intensified CCD camera (Andor Technology) coupled to a spectrograph (MS257 Model 77700A, Oriel Instruments) as the detection system. The TRES were collected using the boxcar technique. The initial gate delay (delay after laser pulse, δt) was set to 500 ns, and the gate width δt was adjusted to 50 μs. The PL was detected in the spectral range 500 nm < λ_{em} < 750 nm with a spectral resolution of 0.08 nm.

The PL decays were analyzed by fitting with a multiexponential function $f(t)$ using the commercial software (OriginPro 8): $f(t) = \sum A_i \exp(-t/\tau_i) + B$, where A_i is the decay amplitude, B is a constant (the baseline offset), and τ_i is the time constant of the decay i.

3. RESULTS AND DISCUSSION

3.1. Structure and Morphology Characterization. Figure 1 shows the TEM and HRTEM pictures of the as-synthesized pure zirconia (ZE) (a, b) and ZEB (c, d). ZE was made up of very small, agglomerated nanoparticles, with a size around 3 nm, as shown in Figure 1a and b. In general, for ZE, no reticular planes were observed from the HRTEM images, which confirmed the amorphous nature of the sample; however, under extensive examination, certain tetragonal (t) and monoclinic-like (m) crystallinity appears to be embedded in the amorphous matrix (Supporting Information, Figure S1). In most of these zones, the d-spacings obtained from the HRTEM images were close to the tetragonal structure, as shown in the inset to Figure 1a with d-spacings of 2.93 and 2.99 Å, consistent with hkl 101, with a theoretical d-spacing of 2.95 Å. However, in some other zones, for example, the one shown in Figure 1b, the d-spacings were more consistent with a monoclinic-like phase, as the d-spacings calculated from the SAED corresponded to hkl $\overline{2}$21, 112, 212, $\overline{2}$12, 202, $\overline{1}$22, and 022 (which correspond to d-spacings of 1.78, 2.02, 1.99, 1.86, 1.69, 1.80, and 1.85 Å of the monoclinic structure). Upon Eu-

bulk doping, similar morphology, size, and structure trends were measured. In addition, the EDX analysis of ZEB is shown in Figure S6 of the Supporting Information, confirming the level of Eu at 1 atomic % with respect to Zr (Supporting Information, Figure S3).

The *in situ* XRD patterns with temperature (between room temperature and 500 °C) for ZEB nanostructures show only broad bands between $2\Theta = 20$ and 40° characteristic of the amorphous state until ~450 °C (Figure 2). At 450 °C, the crystallized metastable t phase (reflection planes at $2\Theta = 29.96$ (111), 35.08 (110), 34.18 (200), 34.92 (002), 50.3 (112), 49.7 (220), 58.64 (131), and 59.62 (113)) is observed. The patterns can be regarded as broadly similar for ZE, ZEB, and ZEI nanostructures which may sustain for the nonsignificant effect of europium addition on the long-range ordering of ZrO_2.
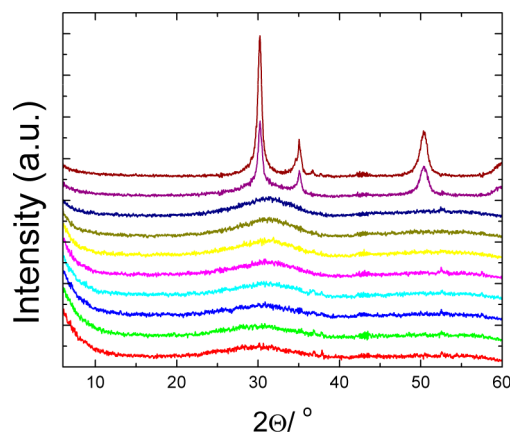
Figure 2. *In situ* XRD patterns with temperature of ZEB nanostructures. Each plot represents a 50 °C temperature increase.

3.2. Local Structure in the Amorphous State. Local structure in the amorphous state of europium-doped (ZEB) and impregnated ZrO_2 (ZEI) was investigated by time-resolved PL spectroscopy. Excitation was performed into the $O^{2-}-Eu^{3+}$ band (around 270 nm, Figure S4a in the Supporting Information) at increasing time delay, δt, ($\delta t = 0.03-15$ ms) after the lamp pulse. The typical emission transitions of europium $^5D_0-^7F_{0-4}$ were observed centered at about ~579, ~592, 612−617, ~653, and ~700 nm among which only the $^5D_0-^7F_{0,1,2}$ are illustrated in Figure 3a−c. The intensity ratio of the hypersensitive electric dipole $^5D_0-^7F_2$ transition and the magnetic dipole $^5D_0-^7F_1$ transition, defined as the asymmetry ratio (R), is used as an indicator of the local asymmetry and/or degree of covalency of the Eu^{3+}−oxygen coordination polyhedron,[37,38] being thus very sensitive to the short-order
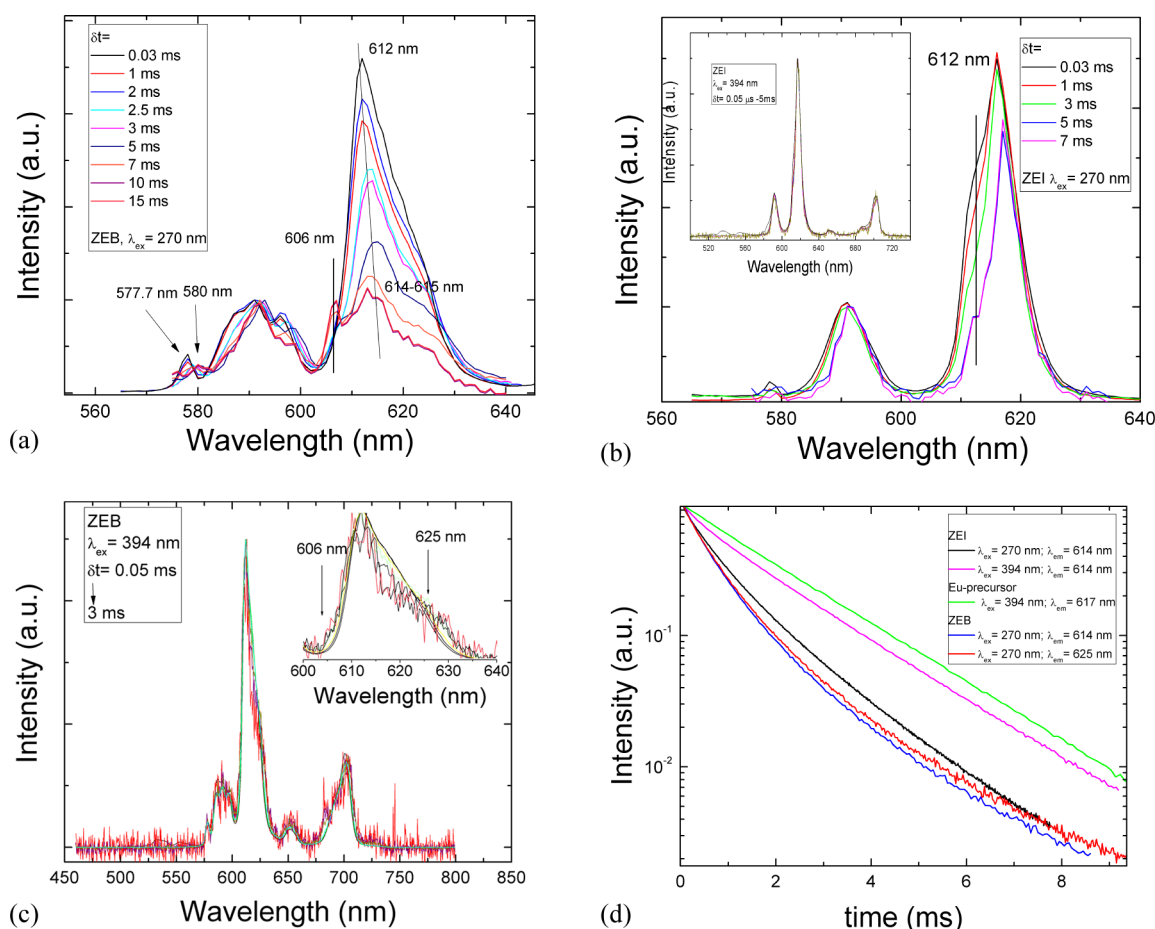
Figure 3. Time-resolved PL spectra of ZEB (a, c) and ZEI (b); PL decays of ZEB and ZEI (d). λ_{ex}, λ_{em}, and δt are indicated in the figures.

effects. It was used to investigate the differences between zirconia crystalline phases, the role of surface coating, the effects of calcination temperature, europium concentration, and incorporation method, the shape effect on the color purity, and so on.[21,22,25−29,39−42] The evolution with time of the asymmetry ratio can also be used as being indicative of the existence of multiple luminescent species or distribution effects as well.[30,35] As illustrated in Figure 3a and b, the time evolutions of the PL spectra of ZEB and ZEI are strongly different. With increasing δt, the emission shape of ZEB is displaying a reduced asymmetry, a narrower $^5D_0-^7F_1$ emission, and a two-peak structure of the $^5D_0-^7F_2$ emission with a new one at 606 nm besides the 612 nm one. Further, a small shift of the emission peak from 612 to 614 nm along with a more pronounced spectral feature at ∼625 nm were observed. The appearance of a narrow 606 nm peaked emission together with the reduced asymmetry ratio in the delayed spectra is strongly indicative of the emergence of a minor, crystalline tetragonal *t* phase.

Because an increased symmetry is decreasing the transition probability of the radiative rate, the europium emission is longer lived for the symmetrical phase being discriminated under increasing δt. A similar trend was obtained under laser excitation into the weak f−f absorption at $\lambda_{ex} = 394$ nm (Figure 3c), albeit the maximum δt was limited at 3 ms because of the poor signal-to-noise ratio (due to the much lower absorption at 394 compared to 270 nm, Figure S4a in the Supporting Information). Nevertheless, it can be concluded that, by using time-resolved PL spectroscopy, a spectral dynamics can be

revealed within the $^5D_0-^7F_2$ emission of amorphous ZEB characterized by (i) minor tetragonal emission, (ii) redshift of the emission maximum from ∼612 to ∼614 nm, and (iii) a spectral feature at about 625 nm.

For the impregnated ZrO_2 (ZEI), the europium ions are expected to reside only on the surface of ZrO_2 which leads to reduced interaction between Eu^{3+} and the ZrO_2 host. As a consequence, the contribution of the broad band assigned to the $O^{2−}-Eu^{3+}$ CT band in the excitation spectra is weaker for ZEI compared to ZEB. Further, the close similarity between the emission spectra of ZEI and europium precursor or europium-2-ethylhexanoate support for the significant contribution of the unreacted Eu precursor in the ZEI sample (Figure S4, Supporting Information). With increasing time delay after the lamp pulse (at 270 nm), the emission is narrowed and the peak value of the $^5D_0-^7F_2$ is red-shifted from 612 to 617 nm which corresponds to the longer-lived emission of europium-2-ethylhexanoate (Figure 3b).

The PL decays of ZEB and ZEI (Figure 3d) were dependent on the excitation ($\lambda_{ex} = 270$ and 394 nm) and emission wavelength ($\lambda_{em} = 614$ and 617 nm) in agreement with the emission properties illustrated above. All decays were nonexponential with two up to three exponentials needed for reasonable fitting. The sources of nonexponentiality can be assigned to the nonradiative emission quenching due to OH and organic groups (see discussion below), heterogeneous distribution, or presence of the unreacted Eu precursor.

3.3. *In Situ* Evolution of Local Structure with Temperature. The in- situ Raman spectra ($\lambda_{ex} = 488$, 514, and 633 nm)
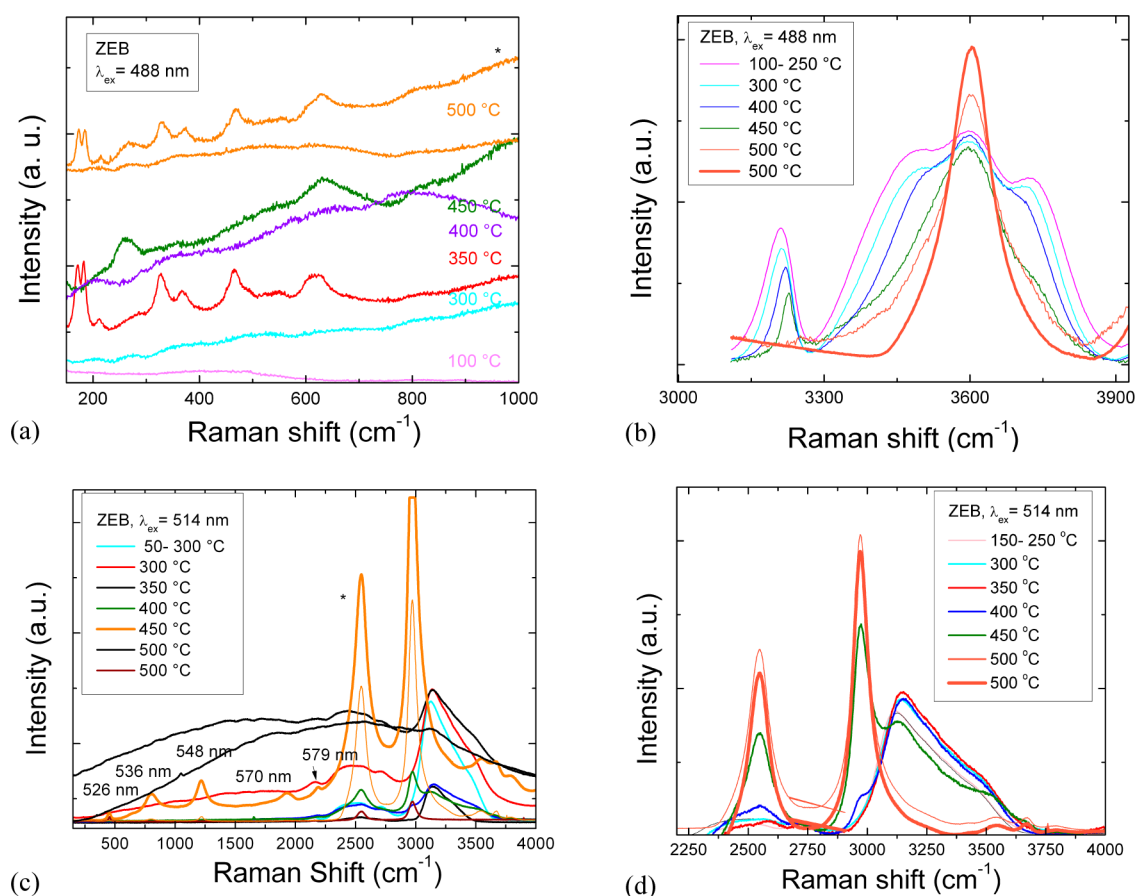
Figure 4. (a) *In situ* Raman spectra (λ_{ex} = 488 nm) of ZEB nanostructures corresponding to ZrO_2 phonon bands; (b) the $^5D_0-^7F_{0,1}$ PL transitions of europium extracted from the *in situ* Raman spectra following background subtraction; (c) *in situ* Raman spectra (λ_{ex} = 514 nm) of ZEB nanostructures; (d) the $^5D_0-^7F_{1,2}$ PL transitions of europium extracted from the *situ* Raman spectra following background subtraction. The thick orange line refers to the spectrum obtained under prolonged calcination (60 min compared to the typical plateau time of 10 min).

measured up to a calcination temperature of 500 °C show a discontinuous evolution of the Raman bands with temperature for ZEB and ZEI nanostructures with significant bands broadening or merging and intensity reducing (Figure 4 and Figure S5, Supporting Information). Despite their complexity, we could trace some general features and trends.

λ_{ex} = *488 nm.* For ZEB nanostructures, both tetragonal and monoclinic crystalline features were detected at temperatures greater than 300 °C, Figure 4. We recall that some tetragonal but also monoclinic crystallites were detected being embedded into the amorphous phase even before calcination (Figure 1). The tetragonal zirconia phase has six Raman peaks.[43−47] The crystal structure of tetragonal ZrO_2 is a body-centered lattice with the space group $P4_2/nmc$,[48] where each Zr^{4+} is 8-fold coordinated with oxygen atoms in D_{2d} symmetry.[44]

The motion of the Zr sublattice is almost entirely responsible for the Raman-active B_{1g} mode at 312 cm^{-1} and E_g mode at 145 cm^{-1}. The highest frequency Raman mode is at 634 cm^{-1} (E_g, asymmetric Zr−O−Zr stretching mode) with a shoulder which is at 600 cm^{-1} (B_{1g}, symmetric Zr−O−Zr stretching mode), whereas the modes detected at ca. 260 and 459 cm^{-1} are A_{1g} and E_g. Around 9 Raman monoclinic bands (from a total of 18) at ∼174, 186, 211, 325, 364, 471, 525, 548, and 613 cm^{-1} were detected. The crystal structure of monoclinic ZrO_2 has a space group of $P2_1/c$,[44] where each Zr^{4+} is 7-fold coordinated with oxygen atoms in low, C_1 symmetry.[44]

The contribution of the *m* phase might be enhanced due to its greater scattering cross section compared to that of the *t* phase.[22] Extending the spectral range to the maximum limit of 4000 cm^{-1}, narrow and relative intense bands were observed around 3610 and 3226 cm^{-1} (Figure 4b). These bands correspond to the europium electronic transitions from the $^5D_0$ excited state, namely, the $^5D_0-^7F_1$ (592 nm) and $^5D_0-^7F_0$ (579 nm) transitions, respectively. Their relative intensities and shapes strongly reveal the increase with temperature of the local symmetry at the europium sites. At 100−250 °C, the europium emission shows a relative strong $^5D_0-^7F_0$ emission and a broadened, three peaks structured $^5D_0-^7F_1$ emission which is typical of amorphous/glassy type emission. At 400 °C, the $D_0-^7F_1$ emission is narrowed and less structured, with the maximum remaining at 592 nm (3610 cm^{-1}) and shoulders around 588.5 and 596 nm (3500 and 3705 cm^{-1}, respectively). The intensity of these spectral features corresponding to the highest and lowest energy of $D_0-^7F_1$ Stark levels is greatly reduced at 450 °C and quenched at 500 °C. The reduction of the intensity related to the $^5D_0-^7F_0$ electronic transition is also a strong indication that the local structure changes from amorphous to higher symmetry crystalline phase. It is interesting to note that, the peak of $^5D_0-^7F_0$ emission is red-shifted by 45 cm^{-1}, while its intensity is reduced from 150 to 500 °C. A similar trend was observed with the ZEI sample (Figure S5, Supporting Information). Correspondence between

Table 1. Correspondence between the $^5D_{0,1,2}$ Electronic Transitions of Europium and Raman Shifts

λ_{ex} (nm)	emission wavelength (nm)/electronic transition/Raman shift (cm^{-1})[b]				
488[a]	579/$^5D_0$–$^7F_0$/3226	592/$^5D_0$–F$_1$/3610	588.5/$^5D_0$–F$_1$/3500[sh]	596.5/$^5D_0$–$^7F_1$/3705[sh]	
514[a]	579/$^5D_0$–$^7F_0$/2187	591.5/$^5D_{0-1}$/2550	587/$^5D_0$–$^7F_1$/2417[sh]	597/$^5D_0$–$^7F_1$/2710[sh]	613/$^5D_0$–$^7F_2$/3150 606.5/$^5D_0$–$^7F_2$/2972
633	714/$^5D_0$–$^7F_4$/1770[w]				

[a]Small differences in emission wavelengths corresponding to $^5D_{0,1}$ transitions extracted at λ_{ex} = 488 and 514 nm are due to background subtraction.
[b]Superscript "w" designates weak intensity lines, and superscript "sh" refers to shoulder features.
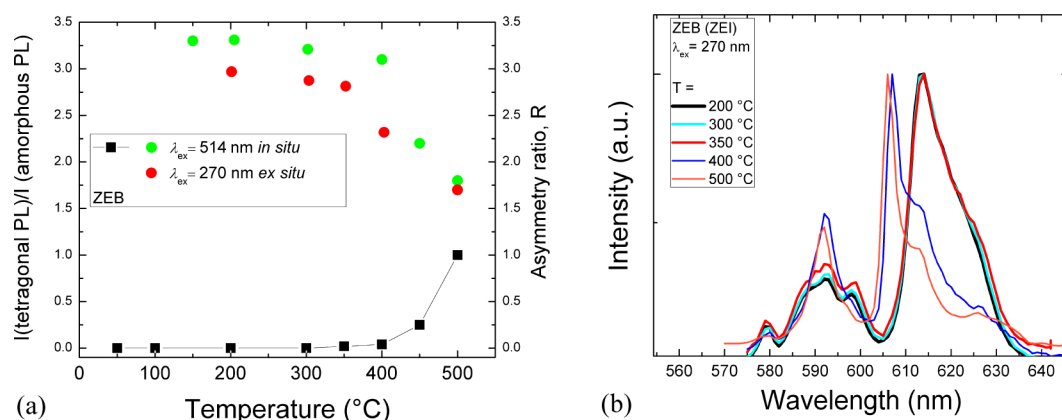
Figure 5. (a) Evolution with temperature of the intensity ratio between tetragonal and amorphous emission (full squares, black color) and asymmetry ratio, R (full circles), extracted from in situ Raman spectra (green color) and ex situ luminescence (red color) of ZEB. (b) Evolution with temperature of the emission for ex situ calcined ZEB.

the $^5D_{0,1,2}$ electronic transitions of europium (nm) and Raman shifts (cm^{-1}) is given in Table 1.

λ_{ex} = 514 nm. At this excitation wavelength, a larger spectral range of europium emission corresponding to the $^5D_0$–$^7F_{0,1,2}$ electronic transitions can be assigned from 2200 to 4000 cm^{-1} Raman shifts (Table 1). Until 400 °C, the emission is dominated by a broad amorphous type emission with $^5D_0$–$^7F_2$ related emission centered around 613 nm (3150 cm^{-1}). However, as early as 300 °C, a small bump can be noticed around 606.5 nm (2972 cm^{-1}) which corresponds to the tetragonal emission of europium. Its intensity relative to the amorphous $^5D_0$–$^7F_2$ emission is only a few percent and remains so up to 400 °C. At 450 °C, the contribution of the tetragonal to amorphous emission is abruptly increased at almost 25%, whereas at 500 °C the emission is predominantly tetragonal. The evolution with temperature of the tetragonal to amorphous emission intensity is illustrated in Figure 5a. This is also reflected in the evolution with temperature of R values which decrease from ~3.3 to ~3 in the temperature interval of 150–400 °C to 2.2 at 450 °C and 1.8 at 500 °C, Figure 5a.

The abrupt change of the Eu–O polyhedra environment is induced by the significant change of the Zr–O bonds upon transition from the amorphous to crystalline tetragonal phase. Recent *ab initio* molecular dynamics simulations on bulk amorphous ZrO$_2$[8] revealed that Zr is mainly 6-fold- and 7-fold-coordinated. It is acknowledged that ZrO$_2$ doped with an oversized trivalent ion (Eu^{3+} has an ionic radius of 1.066 Å compared to 0.84 Å of Zr^{4+} in 8-fold coordination) generates minor host distortion and oxygen vacancies which are supposed to associate with the europium in the next-nearest-neighbor sites,[7] leaving thus 8-fold coordination around europium in tetragonal environment.

λ_{ex} = 633 nm. The evolution of phonon bands with temperature was more or less similar to that observed with 488 or 514 nm excitation (spectra not shown). Both tetragonal and

monoclinic bands were observed between 300 and 400 C, whereas at 450 and 500 °C only the tetragonal bands prevailed. Also, besides the host phonon bands, several lines were detected between 1200 and 2000 cm^{-1} (not shown). In contrast with 488 or 514 nm excitation, the intensity of these extra lines was comparable with that of the phonon bands, being assigned to the $^5D_0$–$^7F_4$ emission of europium which falls in the 685–720 nm spectral range. Because the $^7F_0$–$^5D_0$ transition is strictly forbidden in tetragonal symmetry, the $^5D_0$–$^7F_4$ related emission should originate from europium mainly located in the amorphous sites.

3.4. Ex Situ Evolution of Local Structure with Temperature. To untangle whether the abrupt transition from amorphous to tetragonal type emission is the signature for the *in situ* evolution only, we have also measured the emission spectra of ZEB and ZEI calcined *ex situ* at 100, 200, 300, 350, 400, and 500 °C (λ_{ex} = 270 nm), Figure 5b.

We recall that, for the *in situ* measurements, samples were heated with a rate of 10 °C/min and keeping a plateau of 10 min for collecting the spectra, whereas, for *ex situ* calcination, samples were heated and subsequently cooled with a rate of 1–2 °C/min. Similar to *in situ* measurements, an abrupt increase of the tetragonal to amorphous emission occurred but at lower temperatures (i.e., 350–400 °C compared to 400–450 °C for the *in situ* measurements) which ascertains for the role of thermal history in the crystallization process of doped or impregnated zirconia. No differences between the emission spectra of ZEB and ZEI were obtained at calcination temperatures higher than 200 °C which means that the Eu–O chemical environments are broadly similar in the two samples. Figure 5a also includes the asymmetry ratio versus temperature for the *ex situ* calcined ZEB. The PL decays measured at 614 and 606 nm (corresponding to the maximum intensity of amorphous and tetragonal type emission, respectively) were nonexponential regardless of the calcination

16781

dx.doi.org/10.1021/jp3040538 | J. Phys. Chem. C 2012, 116, 16776–16783

temperature and the average PL lifetimes (τ_{av}) increase with the increase of the calcination temperature. The τ_{av} values of ZEB were calculated using the following formula: $\tau_{av} = \int_{100}^{t_{max}} tI(t)/\int_{100}^{t_{max}} I(t)$ (where $I(t)$ represents the luminescence intensity at time t corrected for the background and the integrals are evaluated within the range of $100 < t < t_{max}$, where t_{max} was typically 25 ms). The values of τ_{av} are 840 μs (λ_{em} = 614 nm) before calcination; 865−870 μs (λ_{em} = 614 nm) at T = 100−200 °C; 880−890 μs (λ_{em} = 614 nm) at T = 300−350 °C; 1.86 ms (λ_{em} = 614 nm) and 3.6 ms (at λ_{em} = 606 nm) at T = 400 °C; and 2.4 ms (λ_{em} = 614 nm) and 3.8 ms (at λ_{em} = 606 nm) at T = 500 °C. The increase of the PL lifetimes with calcination temperature is explained by reduction of the nonradiative energy transfer through the coupling of the $^5D_0$ state of europium to OH and organic groups and growth of the nanoparticles. FT-IR spectra of ZEB (ZEI) exhibit strong absorption bands in the 1300−1600 and 2800−3000 cm^{-1} region due to stretching vibrations of the COO− and CH groups of Zr (Eu) precursors (Figure S6, Supporting Information) which are strongly reduced in intensity following calcination at 500 °C. The relatively broad band at ∼3500 cm^{-1} assigned to the −OH stretching vibrations is also strongly declined, though it can still be observed after calcination at 500 °C. Further, a large surface-to-volume ratio (BET ≥ 300 m^2/g) is measured in the as-syntethized state, whereas the preliminary nanoparticle/crystallite size estimation from HRTEM images and XRD patterns point to a few nm for the amorphous nanoparticles up to 20 nm /10 nm for the tetragonal crystallites obtained on calcination at 500 °C.

3.5. Mechanisms of the *in Situ* Luminescence Excitation. All excitation wavelengths used in Raman experiments (λ_{ex} = 488, 514, and 633 nm) are off-resonant with proximate europium f−f absorption transitions. Excitation energy corresponding to 488 nm is lower by ∼1050 cm^{-1} than the energy corresponding to $^7F_0$−$^5D_2$ absorption. Excitation energy at 514 nm is higher by ∼400 cm^{-1} than the energy corresponding to $^7F_0$−$^5D_1$ absorption and lower by ∼2100 cm^{-1} than the energy corresponding to $^7F_0$−$^5D_2$ absorption. Excitation at 633 nm is off-resonant with the proximate absorption at 579 nm (corresponding to the $^7F_0$−$^5D_0$ transition) with an energy mismatch of ∼1470 cm^{-1}.

Evolution with temperature of intensity of europium emission extracted from the *in situ* Raman spectra is complex, and a detailed description is beyond the scope of the present paper. We only briefly discuss two main factors with opposite influence on this evolution which act superimposed on the amorphous to crystalline (tetragonal) phase transition: (i) the thermal (Boltzmann) population of the upper excited levels ($^7F_2$) which is leading to stronger emission with increasing temperature as a result of increased absorption of the excitation energy. Most probably, the europium emission excited at λ_{ex} = 488, 514, or 633 nm can occur via the upper level $^7F_2$ (located at ∼1000 cm^{-1} above the $^7F_0$ ground level); even its fractional population is slightly below 1% at room temperature. From the $^5D_2$, the europium relaxes to $^5D_0$ via the $^5D_1$ state (λ_{ex} = 488 and 514 nm) or europium is excited directly to $^5D_0$ (633 nm excitation); (ii) the thermal quenching of emission. Generally, the increase of the nonradiative relaxation rate via multiphonon emission leads to a decrease of the emission intensity with temperature. For europium doped in hosts with small energy phonons such as ZrO$_2$, the nonradiative relaxation via multiphonon emission is weak due to the large gap of 12000 cm^{-1} which separates the $^5D_0$ level from the proximate lower

energy $^7F_6$ level. On the other hand, the high-frequency vibrations related to organic groups and adsorbed hydroxyl species combined with the high surface to volume area are very important to account for the low luminescence yield observed before or during the first stages of thermal treatment of europium doped/impregnated ZrO$_2$ nanoparticles.

4. CONCLUSIONS

We have investigated the local structure of europium doped and impregnated ZrO$_2$ nanoparticles in the amorphous state and during amorphous to tetragonal phase transition. The as-obtained nanoparticles grown by oil-in-water microemulsion reaction method were amorphous, with a particle size of ∼3 nm, with some tetragonal (also monoclinic) crystallites embedded in the amorphous matrix. From the *in situ* Raman spectra, the evolution with temperature of europium luminescence evidence for an abrupt increase of the tetragonal relative to amorphous emission, emission narrowing, and decrease of the asymmetry ratio between 400 and 450 °C. For the *ex situ* calcined europium doped and impregnated ZrO$_2$ nanoparticles, a similar trend was observed but the temperature was decreased at 350−400 °C. We have also shown that by using spectrally and temporarily resolved luminescence a spectral dynamics can be revealed within amorphous type emission of europium doped/impregnated ZrO$_2$. In the amorphous state, the effects of the europium addition mode could be differentiated via their emission/excitation spectra and photoluminescence decays. No differences between the Eu−O polyhedra could be observed at calcination temperatures higher than 200 °C. Finally, we envisage that, as europium can be excited off-resonantly under several Vis excitation wavelengths (λ_{ex} = 488, 514, or 633 nm), typically available with micro Raman spectrometers, both Raman and luminescence spectra can be analyzed in a single measurement to enhance information on the local structure of the various hosts during (and after) crystallization.

■ ASSOCIATED CONTENT

ⓢ Supporting Information

HRTEM and STEM pictures, EDS experimental data, and excitation, Raman, and FT-IR spectra. This material is available free of charge via the Internet at http://pubs.acs.org.

■ AUTHOR INFORMATION

Corresponding Author

*E-mail: tiseanuc@yahoo.com.

Notes

The authors declare no competing financial interest.

16782

dx.doi.org/10.1021/jp3040538 | *J. Phys. Chem. C* 2012, 116, 16776−16783

■ REFERENCES

(1) Subbarao, E. C. In *Advances in Ceramics, Vol. 3, Science and Technology of Zirconia*; Heuer, A. H., Hobbs, L. W., Eds.; American Ceramic Society: Westerville, OH, 1981.

(2) Li, P.; Chen, I.-W.; Penner-Hahn, J. E. *Phys. Rev. B* **1993**, *48* (14), 10063−10073; *J. Am. Ceram. Soc.* **1994**, *77*, 118−128.

(3) Yashima, M.; Kato, T.; Kakihana, M.; Gulgun, M. A.; Matsuo, Y.; Yoshimura, M. *J. Mater. Res.* **1997**, *12*, 2575−2583.

(4) Shukla, S.; Seal, S. *Int. Mater. Rev.* **2005**, *50*, 45−64.

(5) Subbarao, E. C.; Maiti, H. S. *Solid State Ionics* **1984**, *11* (4), 317−338.

(6) Garvie, R. C. *J. Phys. Chem.* **1965**, *69*, 1238−1243.

(7) Li, P.; Chen, I.-W. *J. Am. Ceram. Soc.* **1994**, *77*, 118−128.

(8) Zhao, X.; Ceresoli, D.; Vanderbilt, D. *Phys. Rev. B* **2005**, *71*, 085107−085117.

(9) Ward., D. A.; Ko, E. I. *Chem. Mater.* **1993**, *5*, 956−969.

(10) Khan, M. S.; Islam, M. S.; Bates, D. R. *J. Mater. Chem.* **1998**, *8*, 2299−2307.

(11) Chadwick, A. V.; Mountjoy, G.; Nield, V. M.; Poplett, I. J. F.; Smith, M. E.; Strange, J. H.; Tucker, M. G. *Chem. Mater.* **2001**, *13*, 1219−1229.

(12) Minh, N. Q. *J. Am. Ceram. Soc.* **1993**, *76* (3), 563−588.

(13) Ji, Y.; Kilner, J. A.; Carolan, M. F. *Solid State Ionics* **2005**, *176* (9−10), 937−943.

(14) Soares, M. R. N.; Soares, M. J.; Fernandes, A. J. S.; Rino, L.; Costa, F. M.; Monteiro, T. Y. *J. Mater. Chem.* **2011**, *21* (39), 15262−15265.

(15) Fidelus, J. D.; Yatsunenko, S.; Godlewski, M.; Paszkowicz, W.; Werner-Malento, E.; Łojkowski, W. *Scr. Mater.* **2009**, *61* (4), 415−418.

(16) Lange, S.; Sildos, I.; Hartmanova, M.; Aarik, J.; Kiisk, V. *J. Non-Cryst. Solids* **2008**, *354* (35−39), 4380−4382.

(17) De La Rosa, E.; Salas, P.; Díaz-Torres, L. A.; Martínez, A.; Angeles, C. *J. Nanosci. Nanotechnol.* **2005**, *5* (9), 1480−1486.

(18) Salas, P.; Angeles-Chávez, C.; Montoya, J. A.; De La Rosa, E.; Diaz-Torres, L. A.; Desirena, H.; Martiínez, A.; Romero-Romo, M. A.; Morales, J. *Opt. Mater.* **2005**, *27*, 1295−1300.

(19) Chen, L.; Liu, Y.; Li, Y. *J. Alloys Compd.* **2004**, *381* (1−2), 266−271.

(20) Patra, A.; Friend, C. S.; Kapoor, R.; Prasad, P. N. *Appl. Phys. Lett.* **2003**, *83* (2), 284−286.

(21) Gedanken, A.; Reisfeld, R.; Sominski, E.; Palchik, O.; Koltypin, Y.; Panczer, G.; Gaft, M.; Minti, H. *J. Phys. Chem.* **2000**, *104*, 7057−7065.

(22) Kim, B.-K.; Hahn, J.-W.; Han, K. R. *J. Mater. Sci. Lett.* **1997**, *16*, 669−671.

(23) Blasse,G.; Grabmaier, B. C. *Luminescent Materials*; Springer-Verlag: Berlin, 1994.

(24) Dexpert-Ghys, J.; M.; Faucher, M.; Caro, P. *J. Solid State Chem.* **1984**, *54*, 179−192.

(25) Gutzov, S.; Bredol, M.; Wasgestian, F. *J. Phys. Chem. Solids* **1998**, *59* (1), 69−47.

(26) Ghosh, P.; Priolkar, K. R.; Patra, A. *J. Phys. Chem. C* **2007**, *111* (2), 571−578.

(27) Speghini, A.; Bettinelli, M.; Riello, P.; Bucella, S.; Benedetti, A. *J. Mater. Res.* **2005**, *20*, 2780−2791.

(28) Ninjbadgar, T.; Garnweitner, G.; Boärger, A.; Goldenberg, L. M.; Sakhno, O. V.; Stumpe, J. *Adv. Funct. Mater.* **2009**, *19* (11), 1819−1825.

(29) Ehrhart, G.; Bouazaoui, M.; Capoen, B.; Ferreiro, V.; Mahiou, R.; Robbe, O.; Turrell, S. *Opt. Mater.* **2007**, *29*, 1723−1730.

(30) Tiseanu, C.; Parvulescu, V. I.; Sanchez-Dominguez, M.; Boutonnet, M. *J. Appl. Phys.* **2011**, *110*, 103521−103522.

(31) Fornasiero, P.; Speghini, A.; Di Monte, R.; Bettinelli, M.; Kašpar, J.; Bigotto, A.; Sergo, V.; Graziani, M. *Chem. Mater.* **2004**, *16*, 1938−1944.

(32) Otake, T.; Yugami, H.; Naito, H.; Kawamura, K.; Kawada, T.; Mizusaki, J. *Solid State Ionics* **2000**, *135*, 663−667.

(33) Maczka, M.; Lutz, E. T. G.; Verbeek, H. J.; Oskam, K.; Meijerink, A.; Hanuza, J.; Stuivinga, M. *J. Phys. Chem. Solids* **1999**, *60*, 1909−1914.

(34) Sanchez-Dominguez, M.; Boutonnet, M.; Solans, C. *J. Nanopart. Res.* **2009**, *11* (7), 1823−1829.

(35) Tiseanu, C.; Parvulescu, V. I.; Boutonnet, M.; Cojocaru, B.; Primus, P. A.; Teodorescu, C. M.; Solans, C.; Dominguez, M. S. *Phys. Chem. Chem. Phys.* **2011**, *13* (38), 17135−17145.

(36) Sanchez-Dominguez, M.; Liotta, L. F.; Di Carlo, G.; Pantaleo, G.; Venezia, A. M.; Solans, C.; Boutonnet, M. *Catal. Today* **2010**, *158*, 35−46.

(37) Peacock, R. D. *Struct. Bonding (Berlin, Ger.)* **1975**, *22*, 83−121.

(38) Reisfeld, R.; Zigansky, E.; Gaft, M. *Mol. Phys.* **2004**, *102*, 1319−1330.

(39) Ghosh, P.; Patra, A. *Langmuir* **2006**, *22*, 6321−6327.

(40) Soares, M. R. N.; Nico, C.; Peres, M.; Ferreira, N.; Fernandes, A. J. S.; Monteiro, T.; Costa, F. M. *J. Appl. Phys.* **2011**, *109*, 013516−013517.

(41) Smits, K.; Grigorjeva, L.; Millers, D.; Sarakovskis, A.; Opalinska, A.; Fidelus, J. D.; Lojkowski, W. *Opt. Mater.* **2010**, *32*, 827−831.

(42) Yu, L.; Liu, H.; Nogami, M. *Opt. Mater.* **2010**, *32*, 1139−1141.

(43) Feinberg, A.; Perry, C. H. *J. Phys. Chem. Solids* **1981**, *42*, 513−518.

(44) Lopez, E. F.; Escribano, V. S.; Panizza, M.; Carnasciali, M. M.; Busca, G. *J. Mater. Chem.* **2001**, *11*, 1891−1897.

(45) Perry, C. H.; Liu, D. W.; Ingel, R. P. *J. Am. Ceram. Soc.* **1985**, *68*, C184−C187.

(46) Merle, T.; Guinebretiere, R.; Mirgorodsky, A.; Quintard, P. *Phys. Rev. B* **2002**, *65*, 144302−144308.

(47) Fadda, G.; Zanzotto, G.; Colombo, L. *Phys. Rev. B* **2010**, *82*, 064106−064120.

(48) Howard, C. J.; Hill, R. J.; Reichert, B. E. *Acta Crystallogr., Sect. B* **1988**, *44*, 116−120.